DTU Library

Effect of wave nonlinearity on fatigue damage and extreme responses of a semi-submersible floating wind turbine

Xu, Kun; Zhang, Min; Shao, Yanlin; Gao, Zhen; Moan, Torgeir

[Link back to DTU Orbit](#)

Effect of wave nonlinearity on fatigue damage and extreme responses of a semi-submersible floating wind turbine

Kun Xu[a,*], Min Zhang[b], Yanlin Shao[c,d], Zhen Gao[a,e,f], Torgeir Moan[a,e,f]

[a] *Department of Marine Technology, Norwegian University of Science and Technology (NTNU), Trondheim 7491, Norway*
[b] *Shandong Provincial Key Lab of Ocean Engineering, Ocean University of China, Qingdao 266100, China*
[c] *Department of Mechanical Engineering, Technical University of Denmark, 2800 Kgs. Lyngby, Denmark*
[d] *Shipbuilding Engineering Institute, Harbin Engineering University, 150001 Harbin, China*
[e] *Centre for Ships and Ocean Structures (CESOS), NTNU, Trondheim 7491, Norway*
[f] *Centre for Autonomous Marine Operations and Systems (AMOS), NTNU, Trondheim 7491, Norway*

ABSTRACT

Floating wind turbine has been the highlight in offshore wind industry lately. There has been great effort on developing highly sophisticated numerical model to better understand its hydrodynamic behaviour. A engineering-practical method to study the nonlinear wave effects on floating wind turbine has been recently developed. Based on the method established, the focus of this paper is to quantify the wave nonlinearity effect due to nonlinear wave kinematics by comparing the structural responses of floating wind turbine when exposed to irregular linear Airy wave and fully nonlinear wave. Critical responses and fatigue damage are studied in operational conditions and short-term extreme values are predicted in extreme conditions respectively. In the operational condition, wind effects are dominating the mean value and standard deviation of most responses except floater heave motion. The fatigue damage at the tower base is dominated by wind effects. The fatigue damage for the mooring line is more influenced by wind effects for conditions with small wave and wave effects for conditions with large wave. The wave nonlinearity effect becomes significant for surge and mooring line tension for large waves while floater heave, pitch motion, tower base bending moment and pontoon axial force are less sensitive to the nonlinear wave effect. In the extreme condition, linear wave theory underestimates wave elevation, floater surge motion and mooring line tension compared with fully nonlinear wave theory while quite close results are predicted for other responses.

1. Introduction

A significant development of floating wind technology has been witnessed over the last decade. To achieve wind turbines which are safe and serviceable, numerical methods which balance accuracy and efficiency are needed. For instance, high-fidelity numerical methods such as computational-fluid-dynamics (CFD) model and fully nonlinear wave model have been developed to deal with the hydrodynamic loading on wind turbine.

The hydrodynamic analysis of an offshore structure normally consists of determining the sea states at the relevant site depth; selecting applicable wave theory; choosing appropriate hydrodynamic load computation method; calculating structural response. Since offshore wind farms are normally deployed at relatively shallow water area where wave becomes more nonlinear and will lead to a considerable increase of hydrodynamic loads, wave nonlinearity and water depth

therefore are two keywords in the hydrodynamic analysis for both bottom-fixed and floating wind turbine.

Wave nonlinearity according to Gibson and Swan [1], can be divided into higher-order bound nonlinearity and resonant nonlinearity at third order and above. The bound nonlinearities in regular waves are the higher-order terms derived by Stokes [2] which are phase locked to the corresponding linear wave component and intend to sharpen the wave peak and broaden the wave trough. Meanwhile, the resonant nonlinearity tends to redistribute the wave spectral energy by exchanging energy between various wave components when the interaction between wave components satisfies the dispersion relationship. As a result, more spectral energy of nonlinear wave are relocated to higher and lower frequency. Camp et al. [3] investigates the overturning moment of a monopile wind turbine based on linear wave theory and stream function wave at 6 m and 21 m water depths. For the same wave height, significant underestimation is found using linear wave and the

---

* Corresponding author.
E-mail addresses: kun.xu@ntnu.no (K. Xu), violet@ouc.edu.cn (M. Zhang).

difference increases as water depth decreases. Schløer et al. [4] compared the wave loads on monopile foundation using linear and fully nonlinear irregular waves. Redistribution of energy between free and bound components in the nonlinear wave spectra is clearly observed and more energy at the first natural frequency is found in linear wave spectra, which greatly influences the fatigue calculation. For large sea states, the difference between linear and nonlinear extreme wave loads appears to be quite large. The influence of varying water depth on the wave-induced structural behaviour is studied by Li et al. [5] by comparing mooring line tension response at 500 m, 1000 m and 1500 m with same mooring line material. As the water depth decreases, the non-Gaussian property of mooring line tension response increases significantly. Therefore, even stronger non-Gaussianity of mooring line tension is expected for floating wind turbines at shallower water depth. The dynamic structural response of offshore structures in different environmental conditions is the driving factor in the design process. The ultimate structural response and fatigue damage of a spar floating wind turbine has been studied by Li et al. [6]. Mean up-crossing rate method is used to predict the extreme response while S-N curve method is used to calculate the fatigue damage.

The objective of this paper is to investigate the effect of wave nonlinearity by comparing the structural response of a semi-submersible floating wind turbine between linear wave theory and fully nonlinear wave theory. The numerical code to implement fully nonlinear wave kinematics in the irregular stochastic wave train was recently developed and verified by Xu et al. [7]. In this paper, the fatigue damage is calculated for tower base and mooring line in operational conditions and the extreme values are predicted for critical responses in extreme conditions.

2. Methodology

2.1. Floating wind turbine model

The floating wind turbine selected for this study is the OC4 semi-submersible wind turbine at 200 m water depth which was developed in the International Energy Agency (IEA) Wind Task 30 Offshore Code Comparison Collaboration Continuation (OC4) project. The semi-submersible platform consists of four columns connected by smaller pontoons and braces as illustrated in Fig. 1. A NREL 5MW wind turbine is mounted on top whose cut-in, rated and cut-out wind speed are: 3 m/s, 11.4 m/s and 25 m/s respectively. Three catenary mooring lines are connected at the top of the base columns at a depth of 14 m below the still water level. More details about the structure are given in Robertson et al. [8].
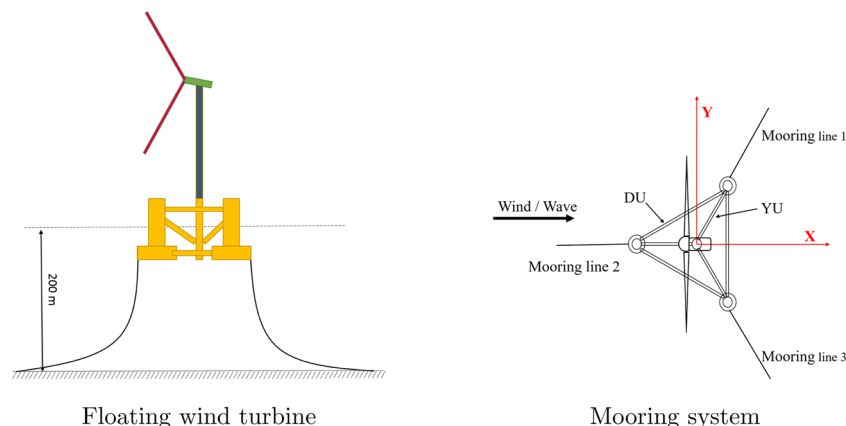
2.2. Fully coupled dynamic analysis

The fully coupled time-domain analysis is performed using HAWC2 (Horizontal Axis Wind turbine simulation Code 2nd generation) which is developed at DTU Wind Energy by Larsen and Hansen [9]. It is able to capture the nonlinear coupling effect from aerodynamics, hydrodynamics, structural dynamics, mooring line dynamics and control system dynamics. The floating wind turbine is divided into several bodies and each body is modeled with a number of Timoshenko beam elements. The turbulent wind field is generated with the Mann model [10]. The hydrodynamic forces acting on the floater and mooring line are calculated based on the Morison's formula.

$$\mathrm{d}F = \rho \frac{\pi D^2}{4} \mathrm{d}z C_M a_n + \rho \frac{\pi D^2}{4} \mathrm{d}z (C_M - 1) a_c + \frac{\rho}{2} C_D D \mathrm{d}z |u_{\mathrm{rel}}| u_{n,\mathrm{rel}} \tag{1}$$

where D is the cylinder diameter, a_n is the undisturbed wave induced acceleration components normal to the cylinder axis, a_c is the normal component of cylinder acceleration, $u_{n,rel}$ is the component of the relative velocity normal to the cylinder, C_M and C_D are the mass and drag coefficients. The wave kinematics of the Morison's equation is provided by an external dynamic link library – *wkin_d ll*. In the original version *wkin 2.4*, importing external wave field is limited to one dimension (vertical) which is intended for bottom fixed wind turbine. It was extended by Xu et al. [7] to two dimensions (both vertical and horizontal) in *wkin 2D* which can apply external wave kinematics on floating wind turbine and its mooring system.

2.3. Wave generation and polynomial fitting

The linear and fully nonlinear irregular waves are generated in the 2D Harmonic Polynomial Cell (HPC) numerical wave tank developed by Shao and Faltinsen [11] and Shao and Faltinsen [12] with linear and fully nonlinear free surface boundary conditions respectively. It was improved by Liang et al. [13] regarding singular flows and discontinuous problems. HPC method is able to solve the velocity potential in each cell by dividing the fluid domain into quadrilateral cells associated with harmonic polynomials. An explicit 4th order Runge–Kutta method is used to update wave elevation and velocity potential on the free surface at each time step. A free surface filter is applied to model nonlinear steep wave to avoid numerical instability.

Because of the large footprint of floating wind turbine, the relevant wave field is also quite large which leads to huge database for the wave kinematics data including wave elevation, particle velocity and acceleration in horizontal and vertical directions. In order to use the kinematics data in HAWC2 and limit the need for memory, the kinematics data at discrete grid points are further processed to polynomial coefficients as shown in Fig. 2. The exact value of wave kinematics is consequently replaced by 2D polynomial coefficients up to a certain order
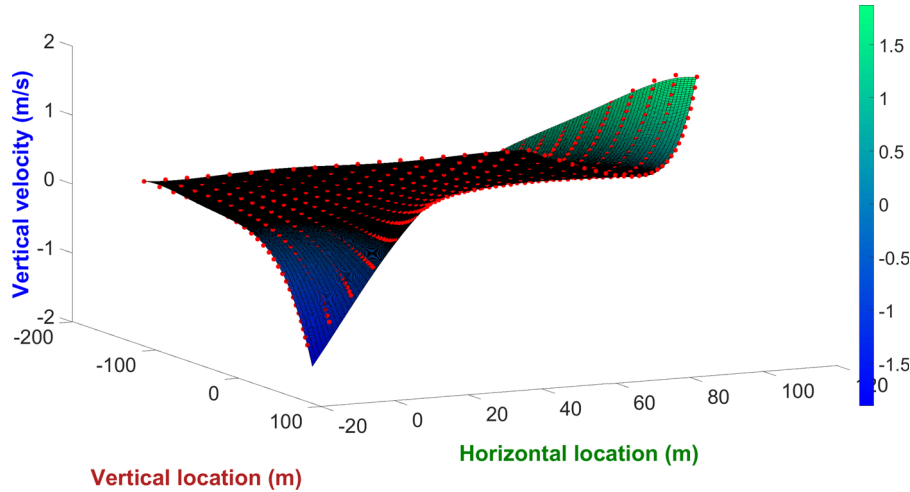

Fig. 1. OC4 semi-submersible floating wind turbine. (a) Floating wind turbine. (b) Mooring system.

Fig. 2. Polynomial fitting of wave kinematics.

with location coordinates as input variables. The details about the polynomial fitting method are described by Xu et al. [7].

2.4. Fatigue damage calculation

Fatigue analysis in frequency domain has been developed and verified with acceptable accuracy and efficiency by Gao and Moan [14]. However, due to the complicated interaction between different parts of the structures and nonlinearity of the response, the fatigue analysis for floating wind turbine is preferably performed in the time domain despite the computational efforts required. A comprehensive fatigue assessment of a semi-submersible floating wind turbine in the time domain has been conducted by Kvittem and Moan [15] which focuses on the influence of simulation length, seed number, wind-wave misalignment, wave-wind dominating role and bin size of environmental conditions on fatigue prediction. However, the irregular wave trains used are based on linear wave theory, therefore the effect due to wave nonlinearity was not studied.

The total structural fatigue damage can be determined as the sum of the fatigue damage that arises from each individual design sea state. The damage for each sea state can be calculated based on Miner-Palmgren hypothesis by adding together the damage from each stress or tension level.

$$D = \sum_{j}^{N_{\text{total}}} \frac{n_j}{N_j} \tag{2}$$

where n_j is the number of cycles at the jth stress range in the time history and N_j is the number of cycles to failure at corresponding stress range according to the design curve. According to Wöhler, the number of cycles until fatigue failure (N) is given by:

$$N = \text{KS}^{-m} \quad \text{or} \quad N = \text{KT}^{-m} \tag{3}$$

where N is the number of permissible cycles of stress or tension range, K is the coefficient in the curve, m is the inverse slope factor and S is the stress range while T is the tension range in the time history. Normally, number of cycles to failure for high level stress cycles is fewer compared to lower level stress cycles. If the applied stress level is below the endurance limit of the material, the structure is assumed to be able to function infinitely. Therefore a two-sloped S-N curve is normally preferred to account for different stress levels.

The fatigue assessment in this paper is carried out in the time domain using Rainflow counting method to count the cycles. The fatigue damage at the tower base due to axial stress is calculated using S-N curve method. The coordinate system for tower base is illustrated in Fig. 3 and the nominal axial stress at tower base for a location (r, θ) is

calculated as:

$$\sigma = \frac{N_x}{A} + \frac{M_y}{I_y} r \cdot \sin \theta + \frac{M_z}{I_z} r \cdot \cos \theta \tag{4}$$

where N_x is the axial force, M_y and M_z are moment about local y- and z-axis respectively, A is the area of the cross section, θ is the angle of the point for fatigue analysis. In general, all locations on the cross section should be considered for fatigue damage calculation. Since wind and wave are aligned in this paper, it is sufficient to take the point on the out radius with $\theta = 270°$ as an example for fatigue evaluation.

The parameter used in the S-N curve is defined as in Eq. (5) and given in Table 1, where N is the number of cycles, t is the thickness, $\Delta\sigma$ is the stress range and the stress concentration factor is set to 1 for simplicity. The fatigue damage for mooring line is calculated using T-N curve method based on API [16]. The parameters defined in Eq. (3) are given in Table 2. The mooring line type studied in this paper is assumed to be studless.

$$\log N = \log \bar{a} - m \log \left(\Delta\sigma \left(\frac{t}{t_{\text{ref}}} \right)^k \right) \tag{5}$$

2.5. Extreme value prediction

Take a random stochastic process $X(t)$ over a time period T as an example. The extreme value of the process is defined as the largest maximum from a sequence of individual maxima

$$X_e = \max\{X_{m1}, X_{m2}, ..., X_{mn}\} \tag{6}$$

where X_e stands for the largest maximum value and X_{mi} represents the individual maxima as shown in Fig. 4. Based on the assumption that all the individual maxima are independent and identically distributed with a common distribution function $F_{Xm}(x)$, the distribution for X_e is described as:

$$F_{Xe}(x) = \text{Prob}\{X_e \le x\} = [F_{Xm}(x)]^n \tag{7}$$

Several methods have been developed for predicting the extreme value distribution, while two of them are used in this paper: type I asymptotic extreme value distribution i.e. the Gumbel fitting method and ACER (average conditional exceedance rate) method.

2.5.1. Gumbel fitting method

When the sample number n is large enough, the extreme value distribution Eq. (7) has been proved that it will converge towards one of three types of distributions: Gumbel, Fréchet and Weibull also known as type I, II and III extreme value distributions whose cumulative
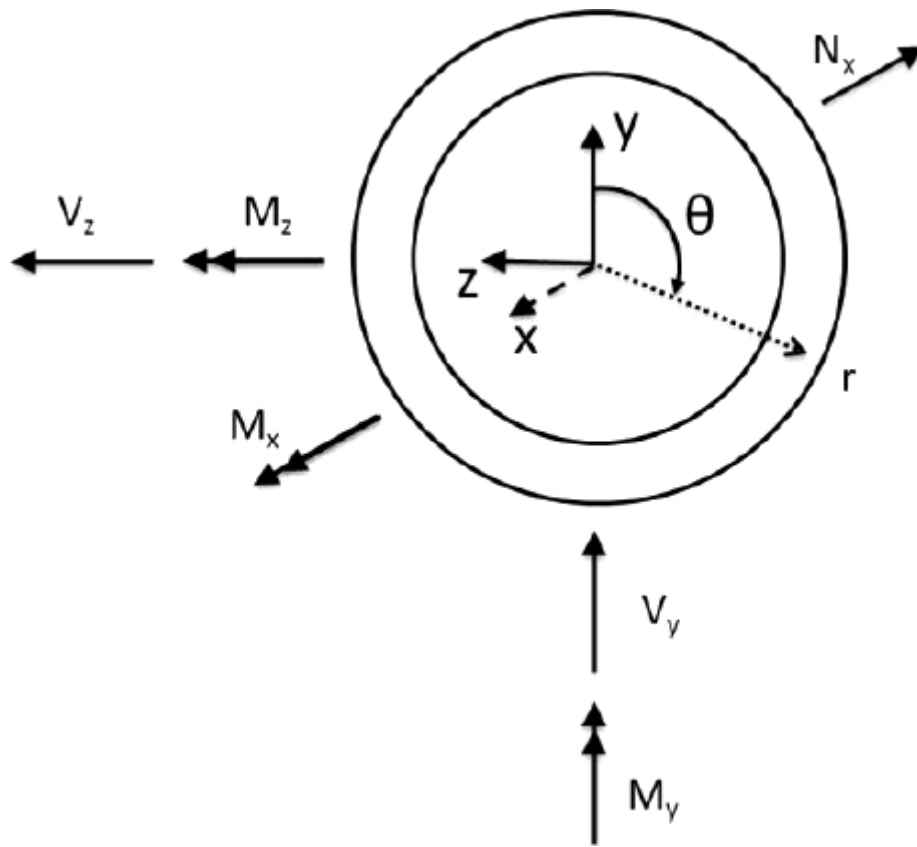
Fig. 3. Coordinate system for tower base fatigue damage calculation.

Table 1
S-N curve parameter for tower base.

$N \leq 10^7$ cycles		$N > 10^7$ cycles		Fatigue limit at 10^7 cycles	k	t_{ref}
m	$\log \bar{a}$	m	$\log \bar{a}$	[MPa]		[mm]
3.0	12.164	5.0	15.606	52.63	0.20	25

Table 2
T-N curve parameter for mooring line.

Component	M	K
Studlink	3.0	1000
Studless link	3.0	316

distribution probability can be assembled as the generalized extreme value (GEV) distribution:

$$F_{\mathrm{Xe}}(x) = \exp\left\{-1 + \gamma\left(\frac{x-\mu}{\sigma}\right)^{-\frac{1}{\gamma}}\right\} \tag{8}$$

Here μ is the location parameter and σ is the scale parameter and γ is the shape parameter. The limiting case when $\gamma \to 0$ will result in the Gumbel distribution which is the most recommended model for marine structures [17].

$$F_{\mathrm{Xe}}(x) = \exp(-\exp(-\alpha(x-\mu))) \tag{9}$$

where α is the scale parameter and μ is the location parameter which can be determined by Gumbel probability paper method. Rewrite Eq. (9) with logarithm of both sides, a linear function is introduced as:

$$-\ln[-\ln(F_{\mathrm{Xe}}(x))] = \alpha(x-\mu) \tag{10}$$

The cumulative distribution probability is represented with a straight line in the probability paper where parameters α and μ can be estimated by the least-square fitting method of the original sample data [18]. An example of Gumbel probability paper for extreme wave elevation is shown in Fig. 5.

2.5.2. Average conditional exceedance rate method

The average conditional exceedance rate (ACER) method proposed by Næss and Gaidai [19] predicts the exact extreme value distribution by building up a sequence of non-parametric distribution functions known as ACER functions instead of the parametric distribution functions. It considers all the global maxima peaks while the dependence between successive peaks in a sampled time-series are taken into account as well which makes it available for both the stationary and non-stationary process. It has been used by Cheng et al. [20] to predict extreme structural responses for floating vertical axis wind turbines.

The extreme value probability distribution according to ACER method is written as:

$$F_{\mathrm{Xe}}(x) \approx P_k(x) \approx \exp\{-(N-k+1)\hat{\varepsilon}(x)\} \tag{11}$$

where k is the order of the ACER function which represents the immediately preceding non-exceedances, $\hat{\varepsilon}(x)$ is the empirical ACER function of order k which is determined by fitting available global maxima peaks from time series [21].

The empirical ACER function follows the form:

$$\hat{\varepsilon}(x) = q_k \cdot \exp\{-a_k(x-b_k)^{c_k}\}, \quad x \geq x_0 \tag{12}$$

Due to the fact that the ACER function behaves close to $\exp\{-a(x-b)^c\}$ in the upper tail region, the coefficients a_k, b_k, c_k and q_k depending on the order k can be determined by extrapolation using mean-square-error function:
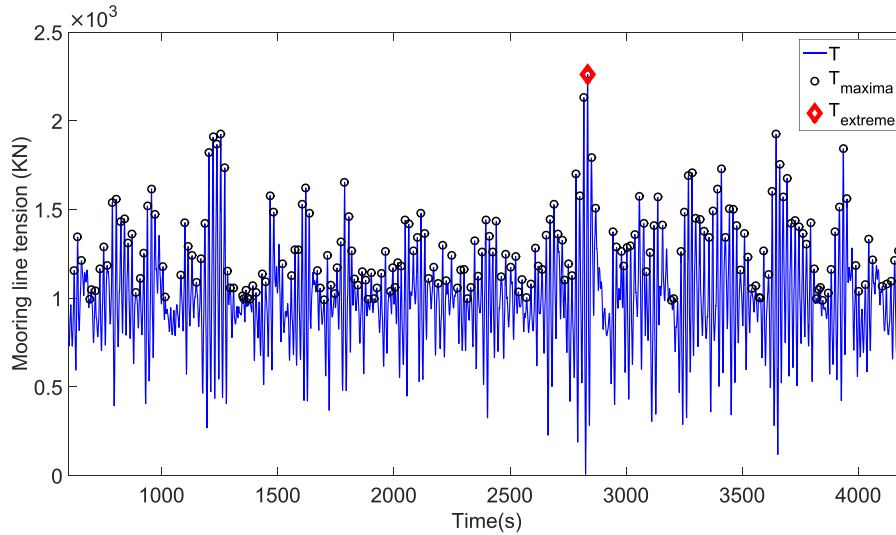
Fig. 4. Global maxima and extreme peak.

$$F(q_k, a_k, b_k, c_k) = \sum_{i=1}^{N} \rho_j |\ln \hat{\varepsilon}_k(x_{\mathrm{mi}}) - \ln q + a(x_{\mathrm{mi}-b})^c|^2 \qquad (13)$$

The weight factor ρ_j is described as $\rho_j = (\ln CI^+(x_i) - \ln CI^-(x_i))^{-2}$ where it represents the 95% confidence interval:

$$CI^{\pm}(x_{\mathrm{mi}}) = \hat{\varepsilon}_k(x_{\mathrm{mi}}) \left\{ \frac{1.96}{\sqrt{(N-k+1)\hat{\varepsilon}_k(x_{\mathrm{mi}})}} \right\} \qquad (14)$$

An example of the ACER function for extreme wave elevation in LC7 condition with linear wave model is given in Fig. 6 representing the empirical ACER function for different orders of k from 1 to 6. The estimated confidence interval for ACER function with $k = 1$ is plotted in Fig. 7.

3. Load cases and environmental conditions

The focus of this paper is to quantify the difference due to wave nonlinearity rather than perform a realistic design of offshore wind turbine, so a series of representative load cases with turbulent wind and irregular wave are selected for the calculation of fatigue load and

extreme load respectively. The environmental conditions are determined based on the wind and wave data at Statfjord site in the Northern North Sea. A joint wind and wave distributions was established by Johannessen et al. [22] considering 1-h mean wind speed at 10 m above sea water level (U_{10}), the significant wave height (H_s) and the spectral peak period (T_p).

$$f_{U_{10}H_sT_p}(u_{10}, h_s, t_p) = f_{U_{10}}(u_{10}) \cdot f_{H_s|U_{10}}(h_s|u_{10}) \cdot f_{T_p|H_sU_{10}}(t_p|h_s, u_{10}) \qquad (15)$$

The joint distribution representing 100-year wind and 100-year wave condition consists of a marginal distribution of wind speed U_{10}, a conditional distribution of H_s for given U_{10} and a conditional distribution of T_p for given U_{10} and H_s. Design wind speed is first determined and the expected significant wave height can then be calculated based on the conditional distribution of H_s for given U_{10} which is a two-parameter Weibull distribution. Likewise, the expected spectral peak period T_p can then be calculated according to the conditional distribution of T_p for given H_s and U_{10} as a log-normal distribution proposed by Johannessen et al. [22].

The wind speed considered in this paper ranges from cut-in, rated and cut-out wind speed with a bin size of 4 m/s. The three dimensional turbulent wind fields are generated using turbulent model by Mann
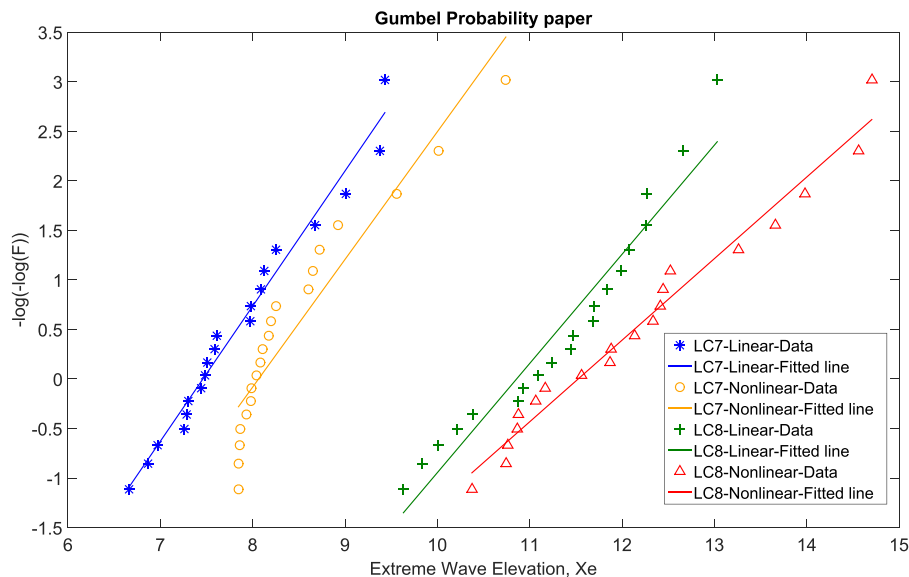

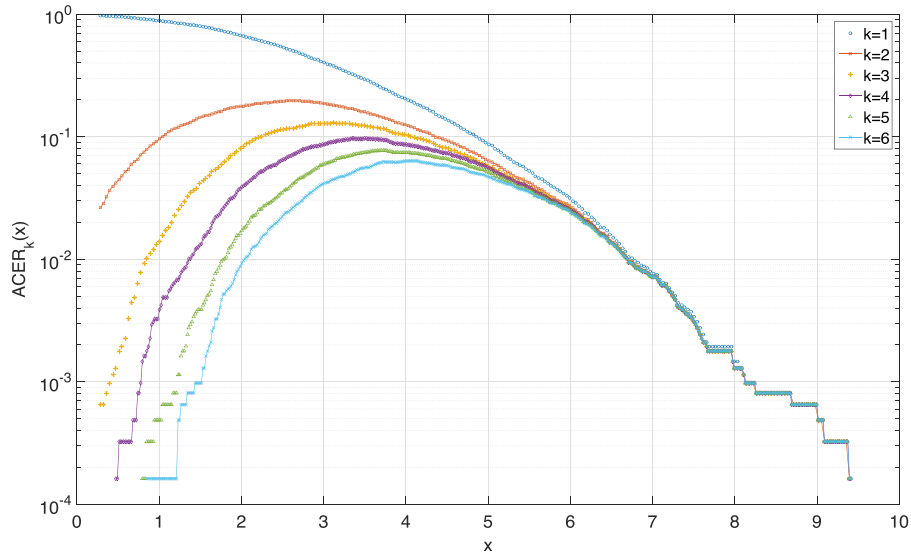**Fig. 5.** Gumbel probability paper for extreme wave elevation.
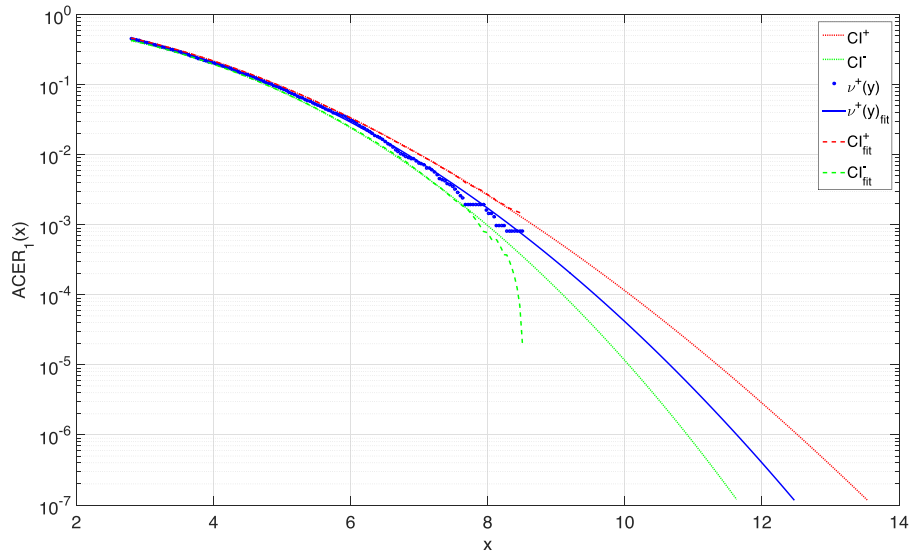
Fig. 6. ACER function for $k = 1, 2, \ldots, 6$.

Fig. 7. Confidence interval for ACER function with $k = 1$.

Table 3
Load cases.

	U_w [m/s]	T_I	H_s [m]	T_p [s]	Seeds	Simulation length [s]	Turbine status
LC1	4	0.258	1.96	9.72	10	4200	Operational
LC2	8	0.174	2.53	9.85	10	4200	Operational
LC3	12	0.146	3.20	10.11	10	4200	Operational
LC4	16	0.132	3.97	10.44	10	4200	Operational
LC5	20	0.124	4.80	10.82	10	4200	Operational
LC5_2	24	0.118	4.80	10.82	10	4200	Operational
LC6	24	0.118	5.69	11.23	10	4200	Operational
LC6_2	20	0.124	5.69	11.23	10	4200	Operational
LC7	40	0.110	9.77	12.95	20	4200	Parked
LC8	60	0.094	15.75	15.10	20	4200	Parked

[10] while the turbulence intensity is determined according to IEC Class C IEC [23]. The vertical wind shear as the variation of the mean wind speed U_z with height z above the ground is considered using the normal wind profile model proposed in IEC [24]:

$$U(z) = U_{\text{ref}} \left(\frac{z}{z_{\text{ref}}} \right)^{\alpha} \tag{16}$$

where U_{ref} is the reference wind speed and z_{ref} is the height of the reference wind speed and α is the power law coefficient. The reference height is set to 90 m above mean water level as the center of rotor and α was chosen to be 0.14 for floating wind turbine based on IEC [24]. The irregular linear and fully nonlinear wave trains are then generated based on JONSWAP spectrum with given H_s and T_p. As a result, a set of load cases with correlated wind and wave are available as given in Table 3. The most probable normal operational conditions with directionally aligned wind and wave are labeled as LCs 1–6 while LCs 7–8 are extreme conditions where wind turbine is under parked condition. In addition, two more operational conditions with specific wind and wave parameters are chosen to study the wind and wave effect labeled as LC5_2 and LC6_2.

All the simulations are run for 4200 s while the transient phase at first 600 s is eliminated to get a 1-h simulation. For the operational conditions, ten different random seeds of wind and wave are applied for each sea states while twenty random seeds of wave are used for the two extreme conditions in order to obtain a proper prediction of the extreme
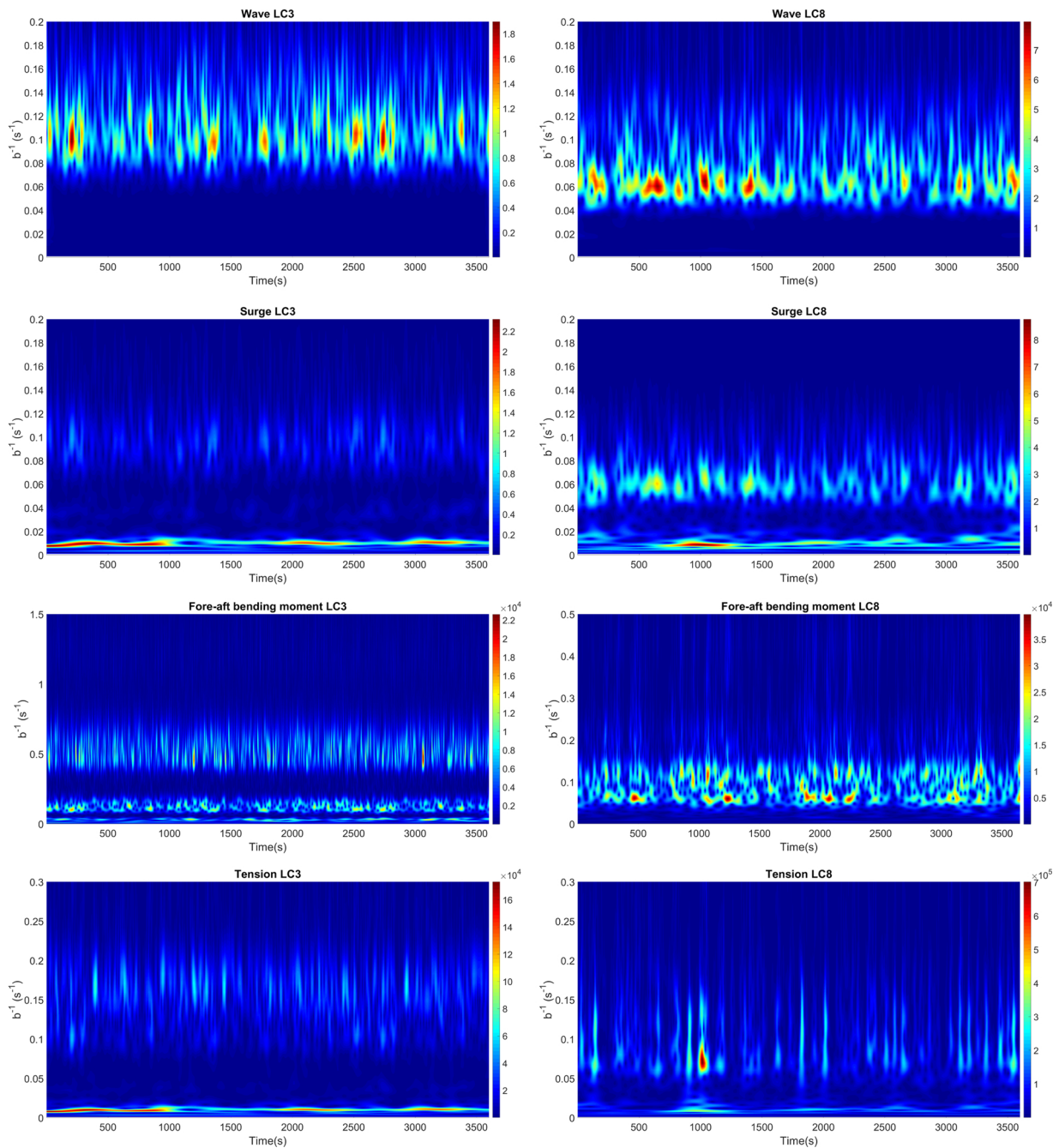
Fig. 8. Wavelet transformation of wave elevation, surge motion, tower base fore-aft bending moment and mooring line tension in LC3 and LC8.

value. The same random seed of wave is used within each load case for the irregular linear and fully nonlinear wave models.

4. Results and discussions

The results of coupled time-domain dynamic simulations are presented and discussed in this section for both operational and extreme conditions. The structural behavior is studied under different load cases in which different load effects are dominating. Same random seed of the irregular wave is used to generate the linear and fully nonlinear wave train to make it possible to investigate the discrepancy due to wave nonlinearity effect. In the following figures, black line represents results due to linear wave and red line represents results due to fully nonlinear wave. The circle marker indicates the mean response with a bar indicating the standard deviation. All the statistics are obtained by

averaging all 10 or 20 one-hour simulations for each load case.

In operational condition where the blades are rotating, the stochastic characteristics of some critical dynamic responses and fatigue damage are studied. As for extreme condition where the wind turbine is parked with blades pitched to feather position, the extreme structural responses are predicted. Above all, the focus of the study is to compare the difference of structural response prediction from linear and fully nonlinear wave.

4.1. Comparison of operational and extreme condition

In operational condition where both wind and wave are functioning, floating wind turbine with turbine rotating behaves quite differently from that in extreme condition with turbine parked. Wavelet transformation which is a contour plot as shown in Fig. 8 illustrates the energy
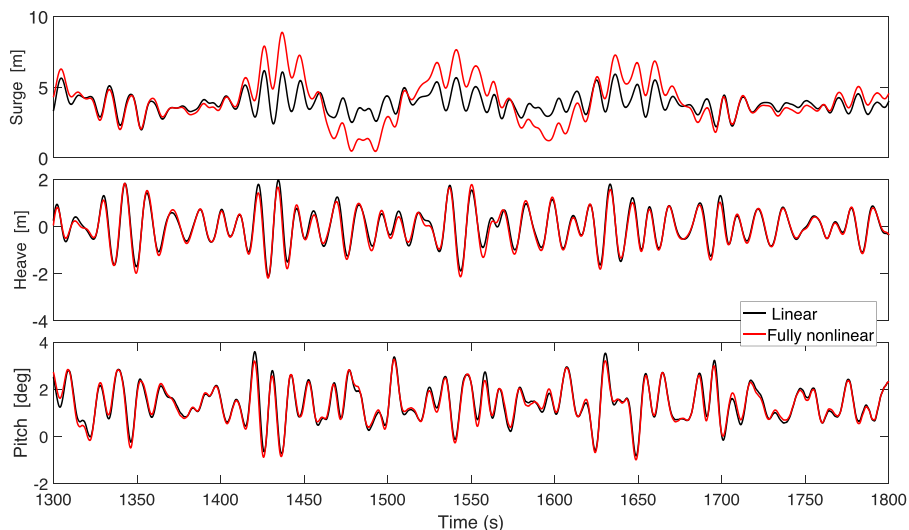
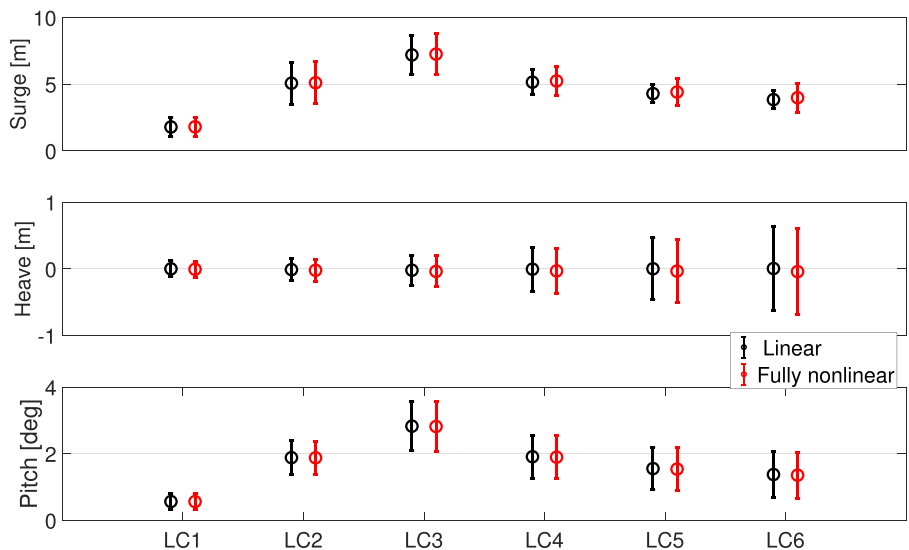**Fig. 9.** Time series of floater motions in LC6.

Fig. 10. Mean and standard deviation of floater motions.
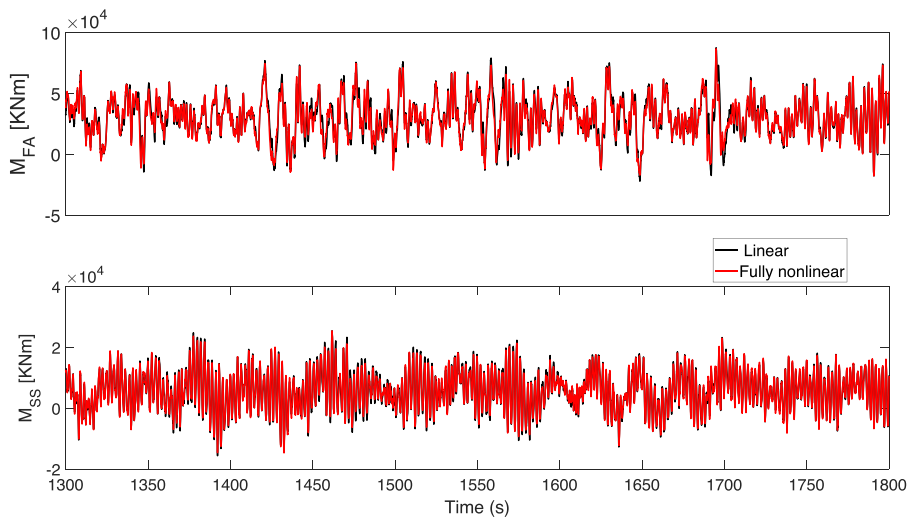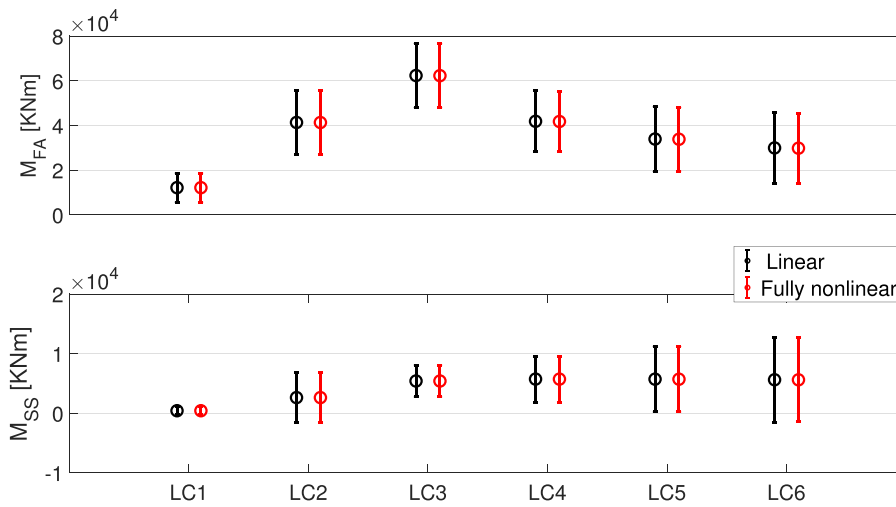

Fig. 11. Time series of tower base bending moment at LC6.

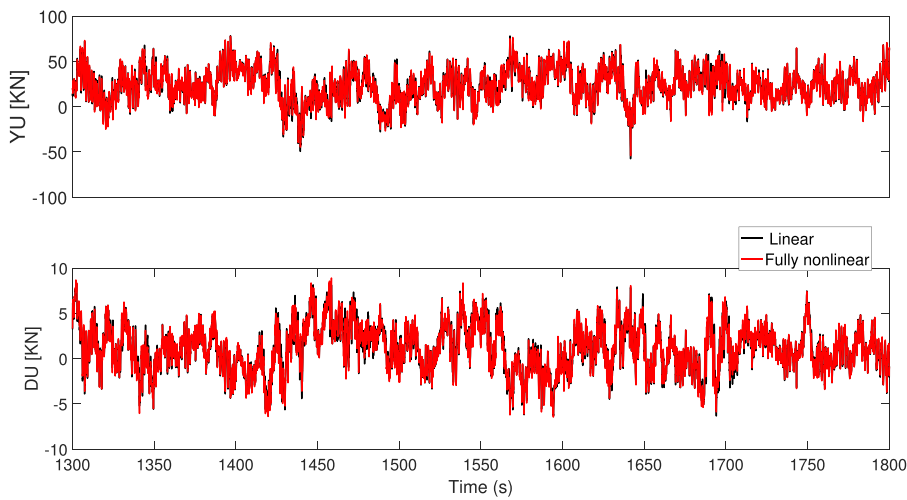**Fig. 12.** Mean and standard deviation of tower base bending moment.

Fig. 13. Time series of axial force in YU and DU pontoon at LC6.
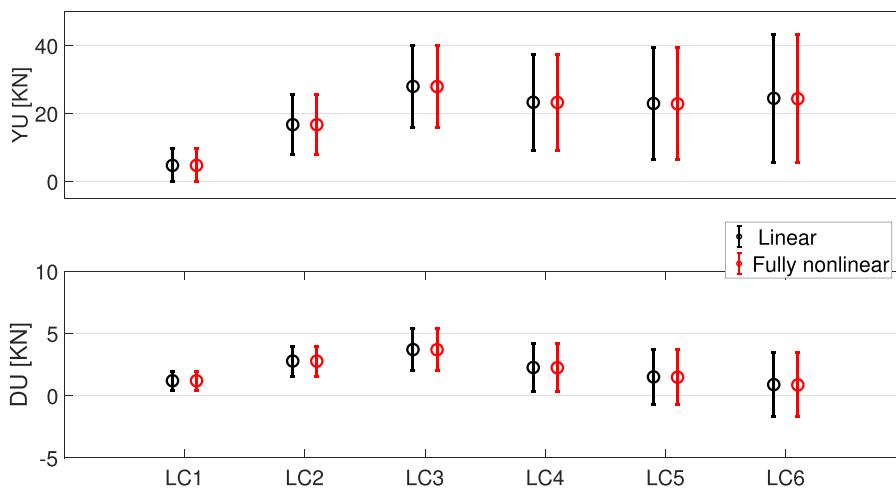

Fig. 14. Mean and standard deviation of axial force in YU and DU pontoon.

distribution of a signal at certain time and frequency with *x*-axis is time and *y*-axis is a scaled parameter which is equivalent to frequency.

From Fig. 8, the energy of surge motion in the operational condition (LC3) is concentrated at low frequency range which is mainly wind-induced while the energy is equally distributed at both wave frequency

and wave-induced low frequency in extreme condition (LC8). Since tower base fore-aft bending moment is quite sensitive to the blade passing (3P) effect and tower natural bending effect in operational condition, the energy of M_{FA} in LC3 is distributed at wind-induced low frequency, wave frequency and higher frequency range. Meanwhile, the
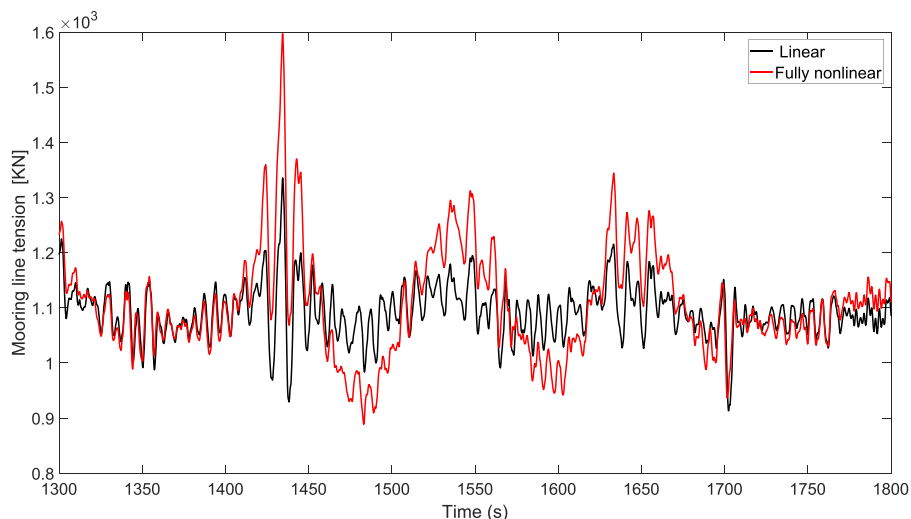
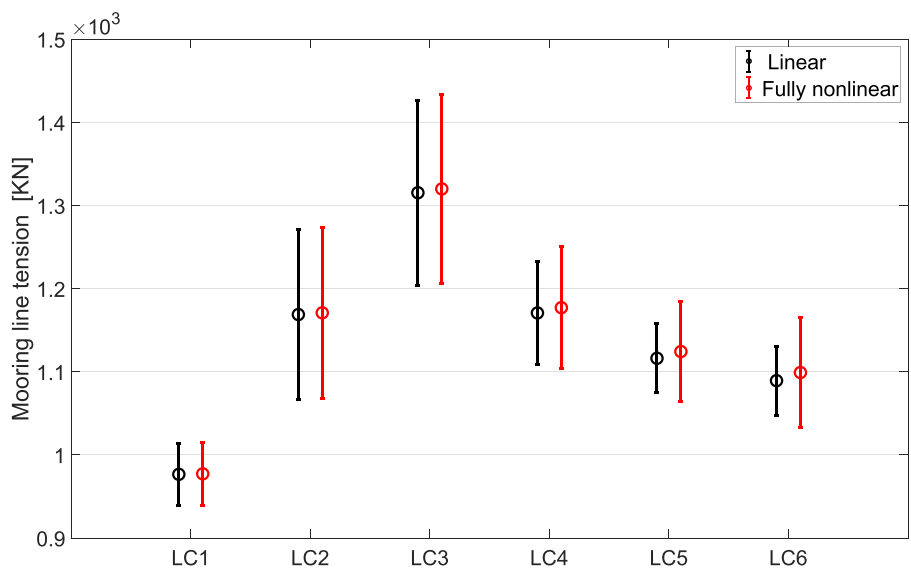**Fig. 15.** Time series of mooring line tension at LC6.

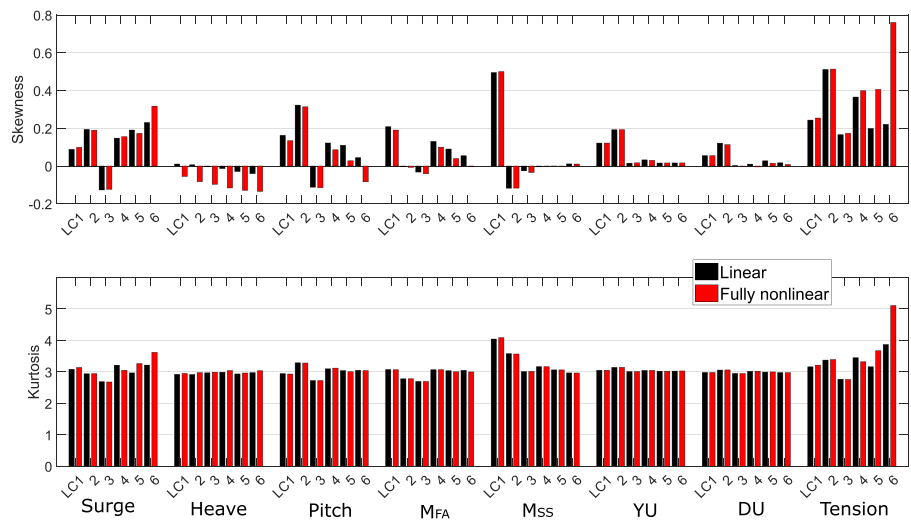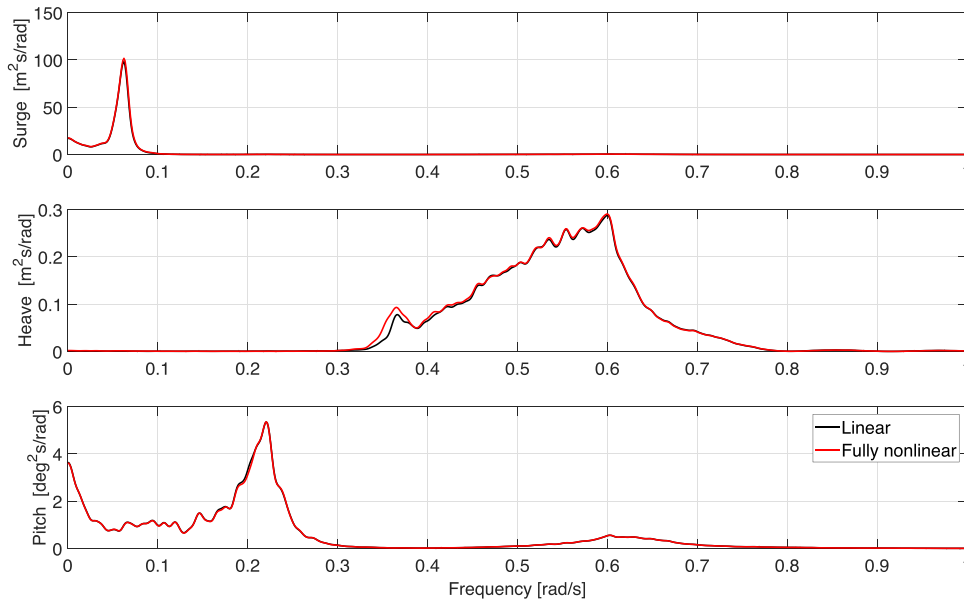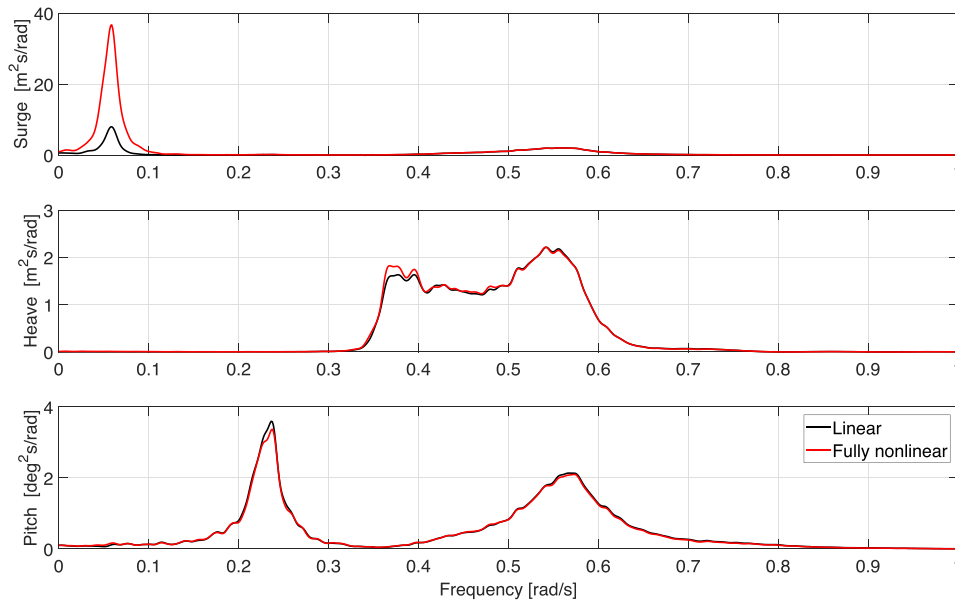**Fig. 16.** Mean and standard deviation of mooring line tension.

Fig. 17. Skewness and kurtosis.

LC3

LC6

Fig. 18. Spectra for floater motions at LC3 and LC6.

energy of M_{FA} is mainly located around wave frequency in extreme condition (LC8) since the turbine is under parked condition. Mooring line tension is mainly affected by surge resonant effect at low frequency in operational condition (LC3) while in extreme condition (LC8), surge resonance and extreme wave contribute equally to the total response.

4.2. Operational conditions

4.2.1. Response statistics
4.2.1.1. Floater motions.
The fact that the configuration of the floater is symmetric and the incoming wave & wind directions are in the symmetric plane leads to negligible sway and roll motion. Therefore the floater motion in surge, heave and pitch are selected as critical

responses to study in this section. The mean value and standard deviation is given in Fig. 10 with an example time series of the motions in LC6 in Fig. 9.

From the time series, floater movement exposed to linear and fully nonlinear wave generally follows the same orbit since same random seed is used for generation of wave and wind respectively. Prediction of heave and pitch are almost the same while significant difference is found for surge motion.

In operational condition where both turbulent wind and irregular wave are considered, surge and pitch motions of the floater are mainly wind dominating while heave motion is primarily wave dominating as shown in Fig. 10. For surge and pitch motion, the mean values are non-zero due to mean wind and wave force. Both mean and standard
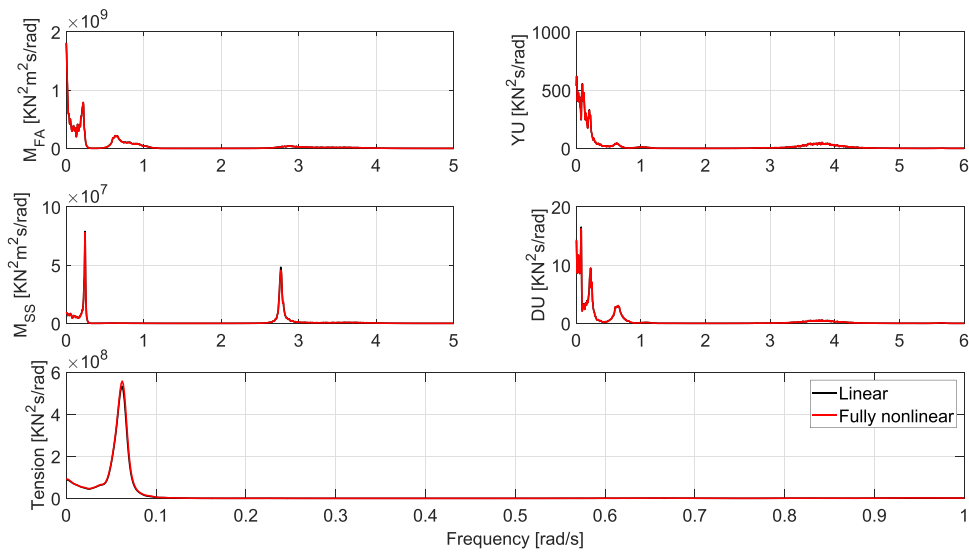
LC3
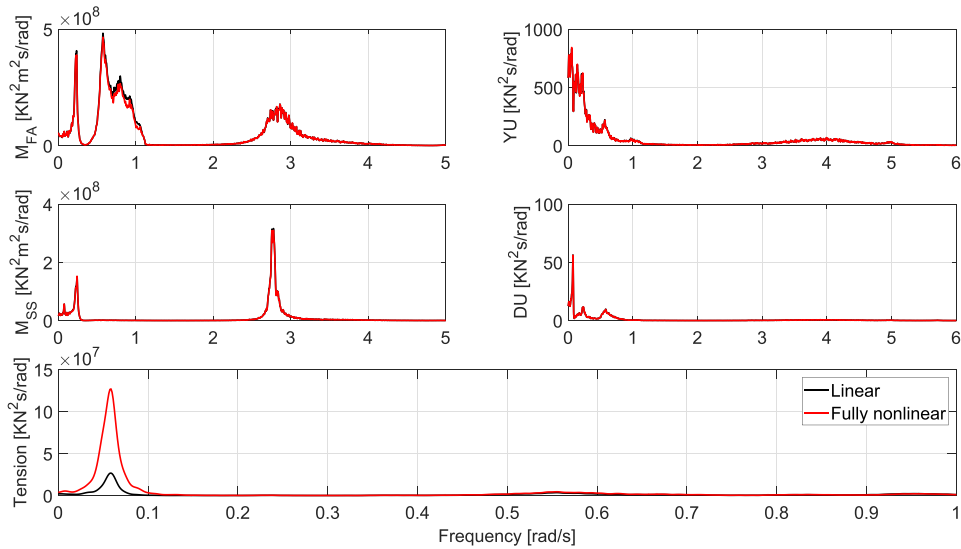
LC6

Fig. 19. Spectra for tower base bending moment, pontoon axial force and mooring line tension at LC3 and LC6.

Table 4
Relevant natural frequencies, unit: [rad/s].

	Surge	Heave	Pitch	3P
Natural frequency	0.054	0.369	0.244	3.79

deviation increase as wind speed increase from cut-in wind speed (4 m/s) in LC1 and reach maximum when wind speed is around rated wind speed (12 m/s) in LC3. As wind speed continues to increase, the blade pitch angle starts to increase due to the activated control system which leads to decreasing thrust force. Accordingly, the mean value of surge and pitch motion start to drop until around cut-out wind speed (24 m/s) in LC6.

As for heave motion, the mean values are close to zero and the standard deviation increases from LC1 to LC6 as the environmental condition becomes more severe, which is mainly wave-induced and it will be explained later in Section 4.2.4. Meanwhile, linear wave

estimates slightly larger heave and pitch response for all LCs while fully nonlinear predicts higher surge response especially in LCs 4–6 where environmental conditions are more severe.

4.2.1.2. Tower base bending moment. The tower base bending moment is mainly due to thrust force acting on rotor and wave excitation force acting on the platform. The fore-aft (M_{FA}) and side-side (M_{SS}) bending moment considered in this paper are parallel and perpendicular to the incoming wind direction respectively. An example of time series and the statistics are given in Figs. 11 and 12.

From the time series, linear and fully nonlinear wave predict quite close result. So are the mean and standard deviation for both (M_{FA}) and (M_{SS}) with slightly higher response from linear wave. The mean value of M_{FA} is mainly affected by thrust force and floater pitch motion, which increases as wind speed increases below rated wind speed and decreases above rated wind speed. The standard deviation of M_{FA} varies not significantly in all LCs except LC1. On the other hand, the mean
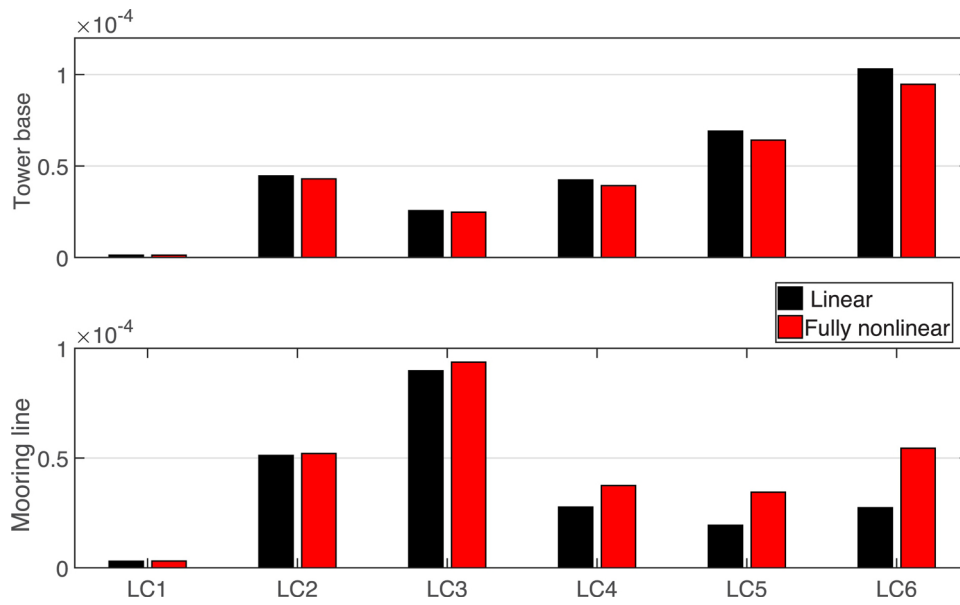
Fig. 20. Hourly fatigue damage at the tower base and the mooring line.
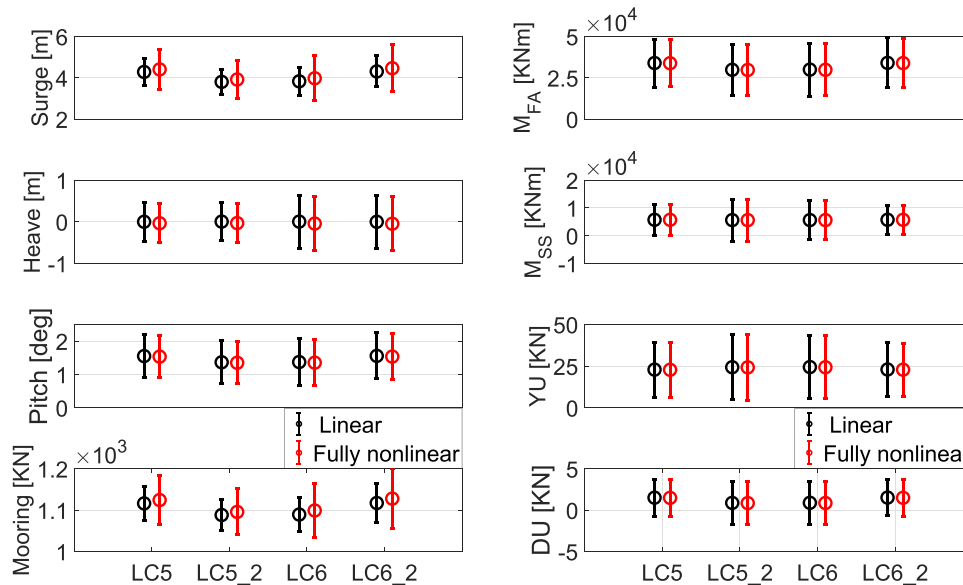

Fig. 21. Response statistics.

value of M_{SS} increases at below rated wind speed and it remains at a constant level as wind speed continues to increase. However, the standard deviation increases as sea state increases and this is mainly wind-induced and it will be discussed in Section 4.2.4. One interesting point to notice is that the bending moment at LC2 uniquely stands out which is due to the excitation of the tower natural bending mode around wind speed of 8 m/s at LC2 and it is more obvious for M_{SS} than M_{FA} as shown in Fig. 12.

4.2.1.3. Pontoon axial force. As shown in Fig. 1, the upper delta pontoon (DU) connecting the offset columns and the upper Y-shaped pontoon (YU) connecting the offset column with main column are studied in this section. The pontoons are modeled with beam elements, it is therefore possible to study the axial force under the load effects due to the external wind and wave and the structural elasticity effect at the ends of the pontoon. Fig. 13 provides an example of the time series of axial force in YU and DU pontoon at LC6.

For conditions below rated wind speed in Fig. 14, the axial force for

both YU and DU pontoons increase as environmental conditions increases. As environmental conditions continue to increase, YU axial force remains at almost the same level while DU axial force starts to decrease. The difference between linear and fully nonlinear wave is not significant, which indicates that the supporting pontoon of the semi-submersible is not sensitive to nonlinear wave effect.

4.2.1.4. Mooring line tension. Among all three mooring lines, the upwind mooring line 2 was selected for study since it is aligned with the incoming wind and wave direction and subjected to the largest tension.

In the operational condition, mooring line tension is directly influenced by floater surge motion and is mainly dominated by low-frequency turbulent wind induced response. Largest mean and standard deviation of mooring line tension occurs in LC3 where wind speed is closest to rated wind speed. It becomes smaller for both lower and higher wind speed as shown in Fig. 16.

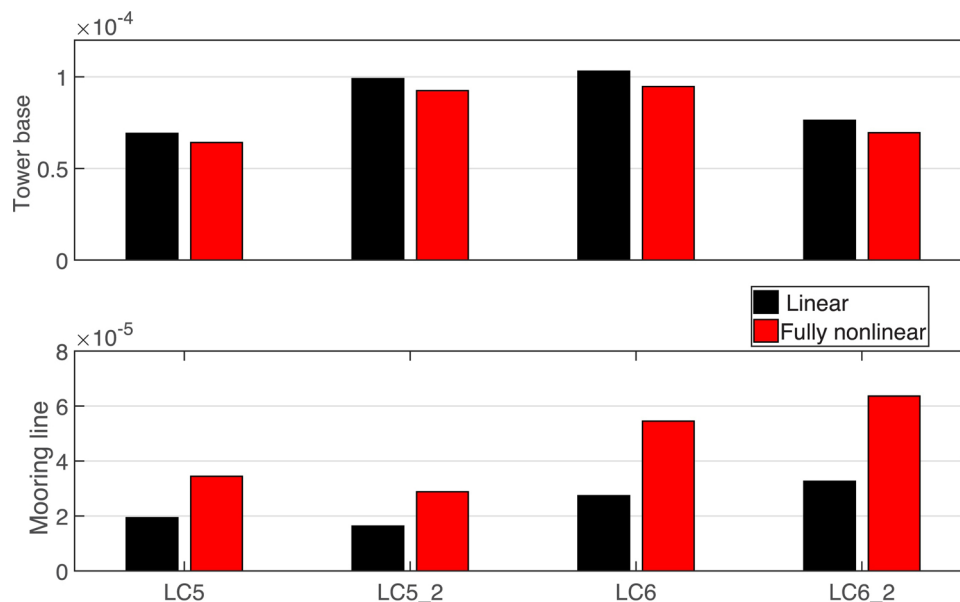Linear and fully nonlinear wave provide quite close predictions of

Fig. 22. Fatigue damage.

the mooring line tension for small sea states (LCs 1–3). However in large sea state, fully nonlinear wave predicts larger response than linear wave and the difference increases as sea state becomes more severe. Quite conspicuous difference is found in LCs 4–6, which proves the significance of wave nonlinear effect at large sea state and the time series in Fig. 15 also shines a light on this discrepancy.

4.2.1.5. Non-Gaussian characteristics. The non-Gaussianity of the response can be characterized by its skewness and kurtosis. Skewness measures the asymmetrical degree of distortion of the distribution from the symmetrical bell curve. Kurtosis on the other hand describes the tailedness of the distribution. The skewness and kurtosis for any univariate Gaussian reponse are 0 and 3 respectively. Positive or negative skewness indicates longer tail on the right or left side. Larger or smaller kurtosis indicates heavy tails with many outliers or light tails with few outliers.

The skewness and kurtosis of all the relevant responses are shown in Fig. 17. Generally all the responses seem quite close to Gaussian process except mooring line tension. As for the comparison between linear and fully nonlinear wave, negative skewness is found for heave motion from fully nonlinear wave, which indicates larger heave response is expected from linear wave and it turns out to be the case. High non-Gaussianity due to wave nonlinearity in large wave is demonstrated by mooring line tension at LC5 and LC6, which lead to higher extreme tension estimation from fully nonlinear wave.

4.2.2. Spectral analysis

Power spectral analysis is used to indicate the contribution of different frequency component. LC3 and LC6 are selected as representative case as one with rated wind speed and one with the largest wave. The power spectra of floater motions are shown in Fig. 18 while the power spectra of tower bending moment, pontoon axial force and mooring line tension are shown in Fig. 19. Wind speeds in LC3 and LC6 are above rated wind speed, therefore the rotor the turbine is operating at its rated rotor speed of 12.1 rpm, which leads to the blade passing (3P) frequency to be around 3.79 rad/s as listed in Table 4.

In LC3 where wind speed is close to rated wind speed, surge resonance dominates surge motion with very little contribution from wave frequency response. Heave motion on the contrary is governed by wave frequency response and a small contribution from heave resonant response. As for pitch motion, the main contribution comes from pitch

resonance and low-frequency wind induced response. Wave frequency response is relatively small. Almost identical power spectra are estimated from linear and fully nonlinear wave in LC3.

First of all, the response amplitude is smaller in LC6. Surge resonant response is also dominating surge motion. However, the contribution from wave frequency response is noticeable and so is the underestimation from linear wave. This is because surge motion is strongly influenced by wave effect at low-frequency where wave nonlinearity is mainly located. Heave resonant component contributes equally as wave frequency component to total heave response. For pitch motion, the low-frequency wind induced response decreases while the response from wave frequency increases.

The spectra for tower base bending moment, pontoon axial force and mooring line tension are illustrated in Fig. 19. The M_{FA} in LC3 is dominated by low-frequency wind induced response. Pitch resonance and wave induced response contribute relatively smaller. M_{SS} on the other hand is mainly influenced by not only pitch resonance but also tower first bending mode and 3P effect. The resonant responses at higher frequency range are larger for M_{SS} since there are limited aerodynamic damping as compared to M_{FA}. Both YU and DU pontoon are mainly influenced by slow varying wind effect, pitch resonance and wave frequency component. The contribution from high frequency component due to tower natural bending mode and 3P effect is relatively small. Almost all the mooring line tension response at LC3 is located at surge resonance range. Close predictions are obtained from the two wave models.

When the wave height increases as in LC6, the contribution from wave frequency response to M_{FA} becomes as important as pitch resonant response. Contribution due to tower natural bending response and 3P effect becomes significant for both M_{FA} and M_{SS}. The main influencing frequency factors for YU and DU axial force are almost the same as in LC3. Surge resonance still dominates the mooring line tension response. However, the difference from the two wave models becomes more significant than in LC3 which indicates that the wave nonlinear effect is important to consider for mooring line response especially for large wave.

4.2.3. Fatigue damage

The fatigue damage of mooring line and tower base is compared in Fig. 20. Generally, the fatigue damage at conditions with lower wind speed and smaller wave than LC1 can be expected not significant. The
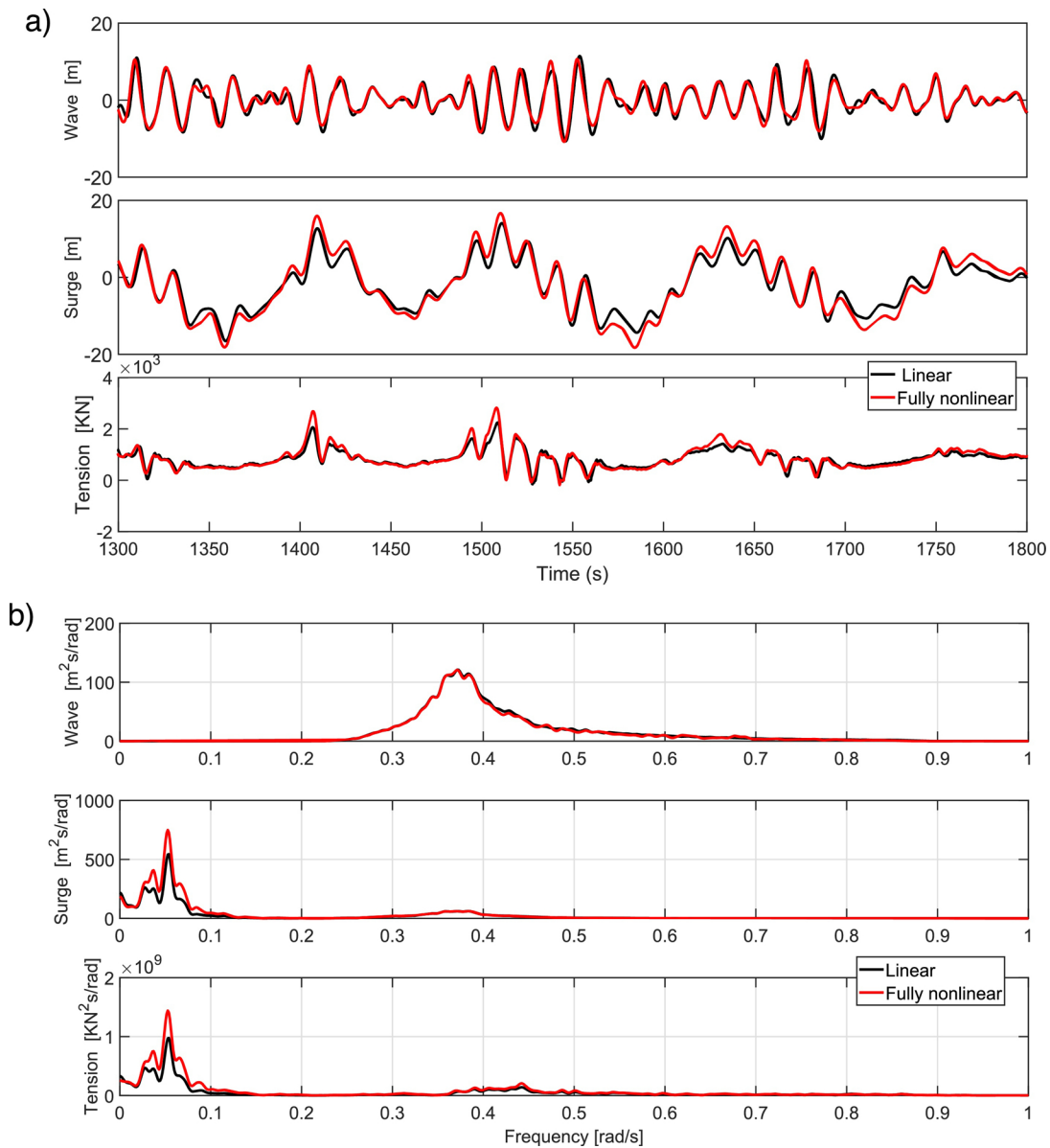
Fig. 23. Time series and spectra for wave elevation, surge motion and mooring line tension in LC7.

fatigue damage at the tower base increases as sea state increases, which is mainly due to increase of wind speed and will be discussed in Section 4.2.4. The excitation of the tower natural bending mode in LC2 significantly increases the fatigue damage level compared with other LCs. Linear wave predicts slightly higher fatigue damage than fully nonlinear wave because more energy is located around wave frequency range for linear wave. However, the difference is not quite significant. Compared with the statistics in Fig. 12, largest mean level of tower base bending moment in LC3 does not necessarily lead to the largest fatigue damage in the tower base.

In general, when exposed to wave only condition, the fatigue damage of the mooring line is proportional to wave height and inversely proportional to wave period [25]. For a given wind speed, fatigue damage tends to increase with increasing wave height and decreasing wave period. From Fig. 20, the fatigue damage level of mooring line follows the same trend as surge response which are wind dominated and reaches the maximum at LC3. From LC4 to LC6, the increase of wind speed actually leads to decreasing fatigue damage while the increase of wave condition on the contrary leads to increasing fatigue damage. The fatigue damage level in LC6 is found to be higher than in

LC4 and LC5, which marks the greater contribution of fatigue damage due to wave than wind. The fatigue damage due to wave nonlinearity effect also increases from LC4 to LC6 as the wave height increases.

4.2.4. Wind and wave load effects

As mentioned before, some responses are mainly wind governed while others are wave dominated. In this section, four representative load cases are selected to distinguish wind-induced and wave-induced response in operational conditions. The same wave conditions are defined for LC5 as LC5_2 and LC6 as LC6_2 respectively while same wind conditions are defined for LC5 as LC6_2 and LC6 as LC5_2 respectively as listed in Table 3. Therefore, wind and wave effect on different responses can be studied comparatively.

The statistics of responses in the four load cases are given in Fig. 21 while the fatigue damage is compared in Fig. 22. When wind speed is above rated wind speed which is the case for the four LCs in this section, the mean and standard deviation of floater surge and pitch motion response in LC5 and LC6 are close to LC6_2 and LC5_2 respectively, which proves that both of them are wind-dominated while the influence from waves is less significant. For heave motion, the reversed result proves
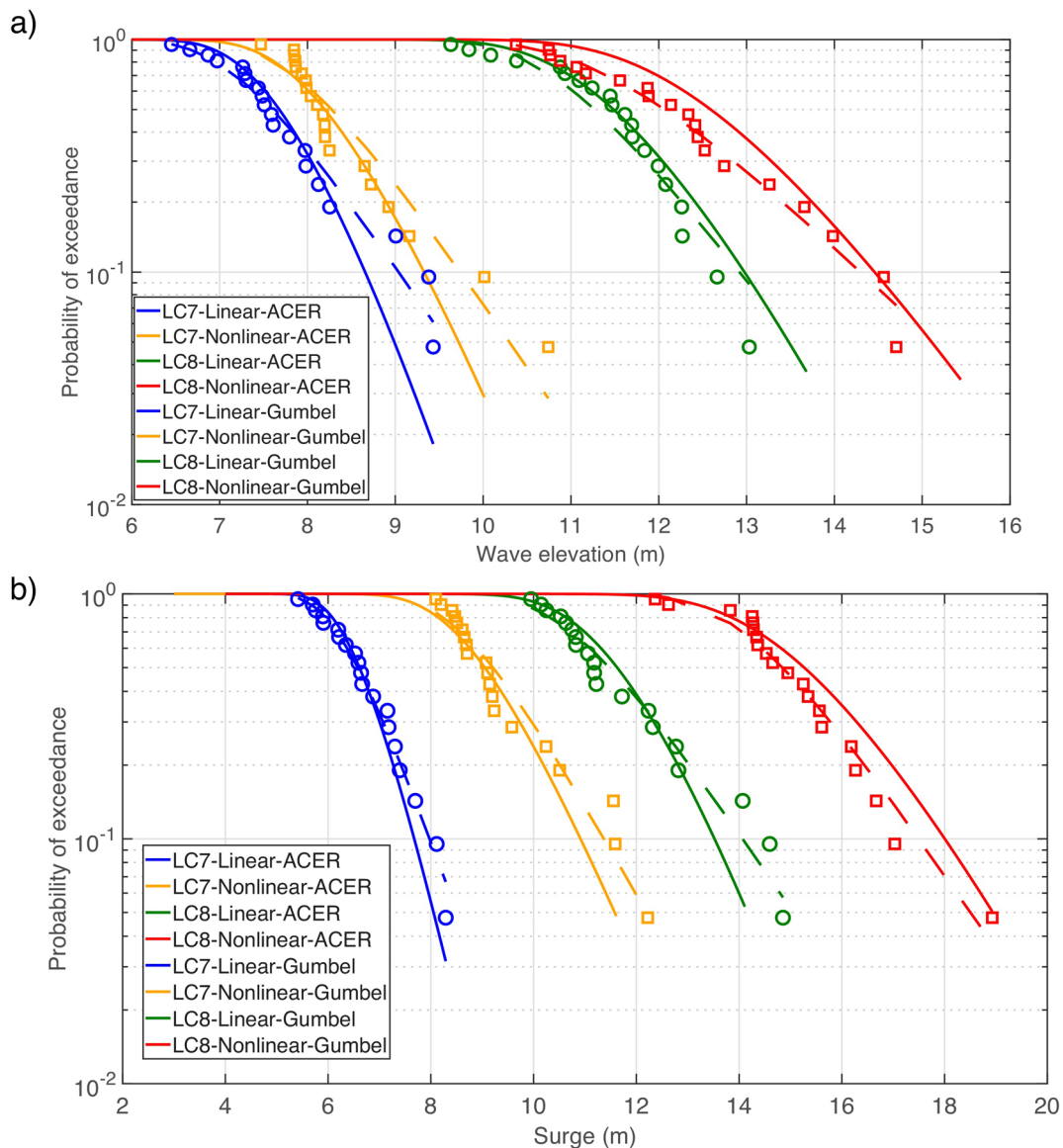
Fig. 24. Exceedance probability for wave elevation and surge motion. (For interpretation of the references to color in the text, the reader is referred to the web version of this article.)

that it is mainly affected by wave effects. As for the tower base bending moment and axial force in YU and DU pontoon, they are all wind-governed response based on close prediction from LC5 as LC6_2 and LC6 as LC5_2. However, the wave nonlinearity effect calculated as the difference between fully nonlinear wave and linear wave is found to be the same for LC5_2 as LC5 and LC6_2 as LC6 where the same wave condition is applied within each pair. As for mooring line tension, the mean value and standard deviation is wind dominating.

The fatigue damage level at tower base is mainly affected by wind effect as shown in Fig. 22. Generally speaking, wind is also dominating the fatigue level for mooring line at below rated wind speed where wave condition is small too. However, the contribution from wave becomes comparable to influence the total fatigue level at above rated wind speed when the wave is normally large too. Therefore, LC6_2 and LC6 with larger wave lead to clearly larger fatigue damage than LC5 and LC5_2. Meanwhile, the amplitude of wave nonlinearity effect is related to wave parameter too.

4.3. Extreme conditions

As concluded in operational condition, floater surge motion and mooring line tension are relatively more sensitive to wave nonlinear effect compared with other responses. Fig. 23 gives a corresponding example of time series and spectra in extreme condition (LC7) where the wind turbine is under parked condition and the wave load effect is dominating compared with wind load which mainly provides a drag force on the blades and tower. Clear difference is found from the two wave models. In extreme conditions (LC7 & LC8), the extreme value for the critical responses will be predicted in this section based on the Gumbel fitting method and ACER method as mentioned in Section 2.5.

As for Gumbel fitting method, the maximum value identified in the 20 simulations with 1-h effective duration with different random seeds are plotted in Gumbel probability paper as shown in Fig. 5. Then the shape and location parameters are determined accordingly. Once the unknown coefficients are estimated, the probability distribution function for Gumbel distribution is available. A large simulation sample is required in order to predict the Gumbel distribution with acceptable accuracy. Meanwhile, only the largest maxima is used for estimation
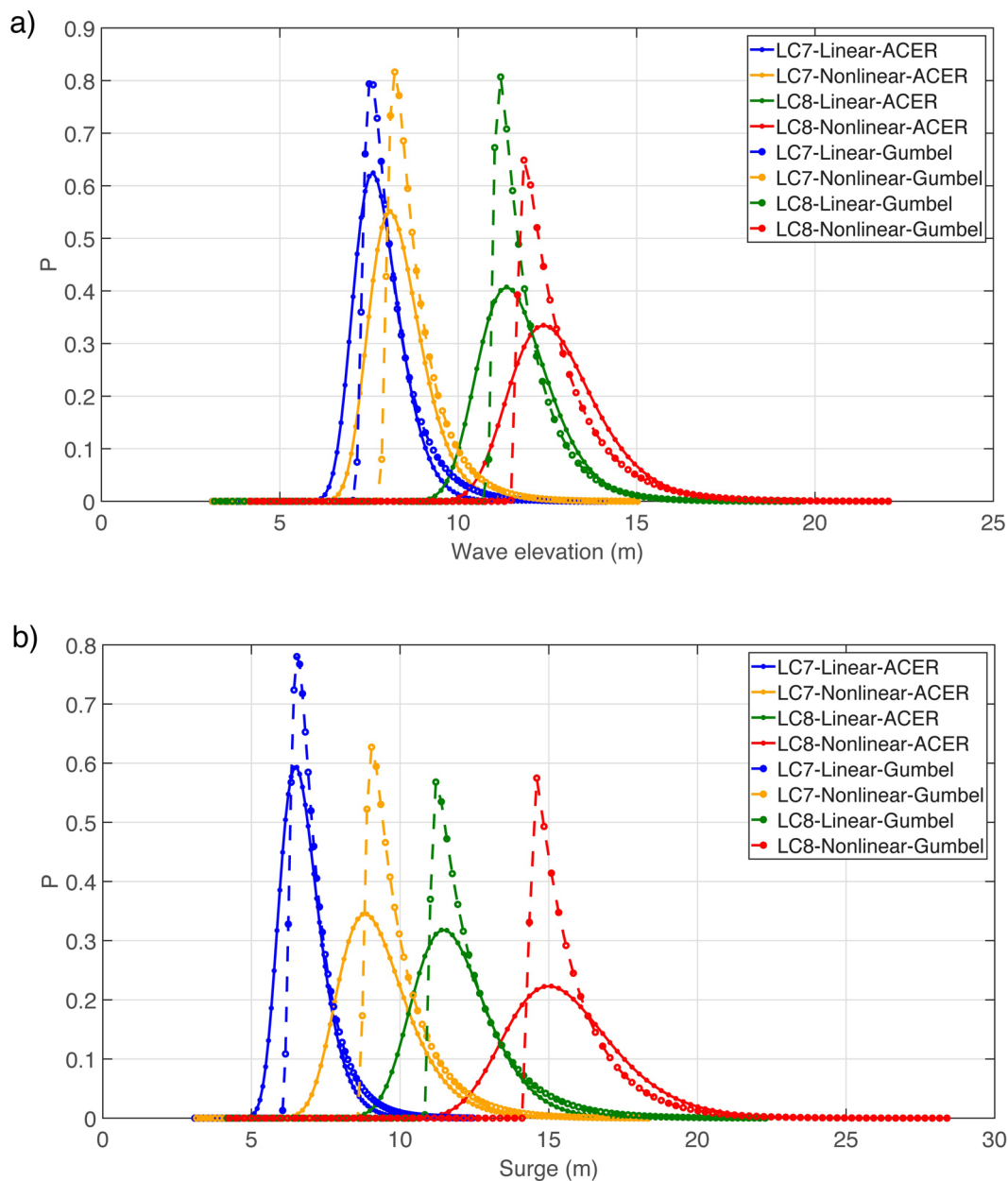
Fig. 25. Probability density function of extreme wave elevation and surge motion.

while the other maxima peaks did not really contribute.

Different from the Gumbel fitting method, all individual peaks as shown in Fig. 4 are involved in ACER method for predicting the extreme value. In addition, all the peaks from the 20 simulations are utilized while the number of exceeding peaks per hour is taken as the total number of peaks divided by the number of seeds. The empirical ACER function, $\hat{\varepsilon}_k(x)$ with order k from 1 to 6 is plotted in Fig. 6. Noticeable variation of ACER function with different order is discovered at lower range of the individual maxima indicating the significant dependence between data points. However, the variation disappears in the tail region for all functions which allows the first-order ACER function $\hat{\varepsilon}_1(x)$ to be chosen for extrapolation which involves most data for estimation and offers same level of accuracy as higher order functions at the same time. Meanwhile, the empirical ACER function in the tail region is close to a straight line which indicates the applicability of Gumbel distribution to describe the extreme value in this study because Gumbel distribution will be illustrated as a straight line in ACER plot ideally. The empirical function $\hat{\varepsilon}_1(x)$ is presented in Fig. 7 including the 95%

confidence interval fitted by time series peaks as well as the estimation from extrapolation scheme. Previous studies by Fu et al. [21] show that the prediction is not sensitive to the choice of the tail marker x_0 which is used to define the tail region, therefore the default value is chosen. Finally, the extrapolation scheme leads to the estimation of all the coefficients required in ACER function.

Once all the coefficients for both methods are determined, the one-hour exceedance probability is plotted in Fig. 24 for wave elevation and surge motion where the solid line represents ACER function and dashed line stands for Gumbel function while original maximum peaks from each simulations are shown as markers with different colors. Exceedance probability not only indicates how well the probability models fit with original data but also provides a direct way to determine the extreme value over a certain probability occurrence level. In general, linear wave models predicts smaller extreme value than fully nonlinear wave model for a given exceedance level while the predictions from ACER method and Gumbel method are pretty close to each other.
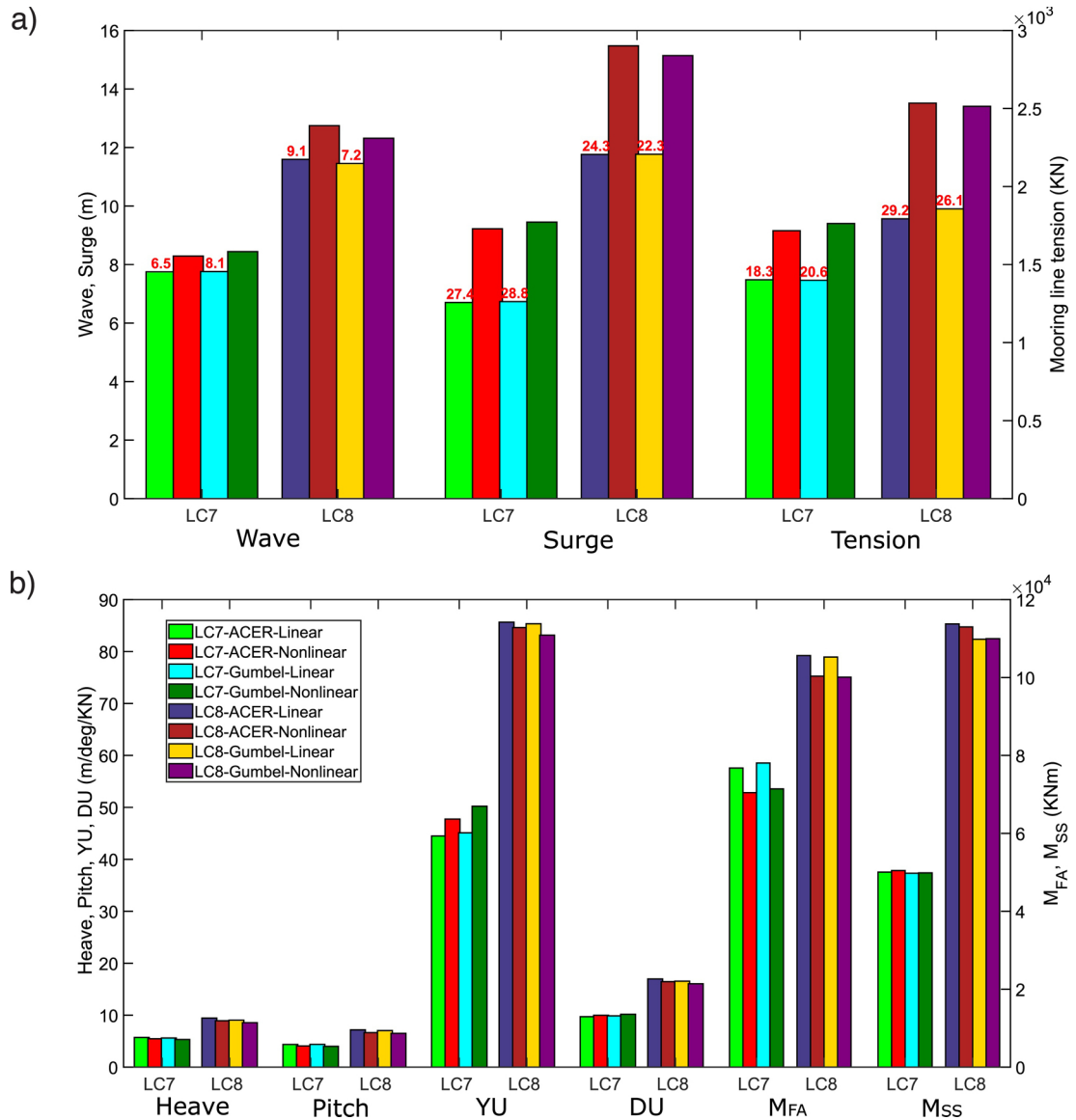
Fig. 26. Extreme response (The red numbers on top of the bar column quantify the under-estimation of linear wave theory as the percentage of the difference to the results of fully nonlinear wave theory). (For interpretation of the references to color in this figure legend, the reader is referred to the web version of this article.)

Meanwhile, the probability density functions can also be derived respectively from Eqs. (9) and (11) and plotted in Fig. 25:

$$f_{\text{Gumbel}}(x) = \alpha \cdot \exp(-\alpha(x - \mu) - \exp(-\alpha(x - \mu))) \qquad (17)$$

$$f_{\text{ACER}}(x) = (N - k + 1) \cdot q \cdot a \cdot c \cdot \exp\{-(N - k + 1) \cdot q \cdot \exp[-a(x - b)^c] \\ - a(x - b)^c\} \cdot (x - b)^{c-1} \qquad (18)$$

Accordingly, the expected maximum value for both methods can be expressed as:

$$E_{\text{Gumbel/ACER}}[X] = \int x \cdot f_{\text{Gumbel/ACER}}(x) \mathrm{d}x \qquad (19)$$

The expected extreme values are predicted for all the relevant responses as shown in Fig. 26 where different colors are used to represent the predictions from two methods in two load cases. The responses which are sensitive to nonlinear wave effect are distinguished from others.

First of all, as wave height increases, the extreme response due to higher sea states (LC8) is predicted larger than smaller sea states (LC7). Secondly, Gumbel fitting method generally predicts quite close results as ACER method for all cases even though latter method utilizes more

data from time series. Most importantly, linear wave model significantly under-predicts extreme floater surge motion and mooring line tension compared with the fully nonlinear wave model for both LC7 and LC8 conditions and it becomes more significant as sea state becomes more severe. Underestimation is found for wave elevation, surge motion and mooring line tension with approximately 10%, 25% and 25% respectively. Meanwhile, the extreme value predictions are quite close for other responses.

5. Conclusions

This paper investigates the hydrodynamic behaviour of floating wind turbines based on linear and fully nonlinear wave kinematics theory. Several load cases are considered including operational conditions with turbine rotating and extreme conditions with turbine parked. Fatigue damage has been calculated and extreme values have been predicted by Gumbel fitting method and ACER method. Representative load cases are selected to distinguish wind-induced and wave-induced response.

In operational conditions, the floater heave motion is mainly wave-induced and increases as wave becomes larger while wind effect is

governing surge and pitch motion which reaches maximum when the wind speed is close to rated wind speed. Linear wave theory predicts slightly higher heave and pitch motions while the fully nonlinear wave theory predicts larger surge motion and the difference increases significantly as the wave height increases. This is because wave energy is redistributed to the higher and lower frequency range than wave frequency due to wave nonlinearity effects and it greatly influences surge motion whose natural period is in the low frequency range. The tower base bending moment in both fore-aft and side-side direction is more influenced by wind-induced thrust force. The excitation of tower natural period increases the response level significantly. However, the bending moment estimates from the two wave theories are quite close with slightly larger value from the linear wave theory since it contains more energy around wave frequency range. The axial forces in YU and DU pontoon are mainly influenced by slowly varying wind effect, pitch resonance and wave-frequency response, while the wave nonlinear effect is not significant. Mooring line tension is mainly influenced by floater surge resonance and considerable contribution comes from wave frequency range when wave is large, therefore the tension reaches the maximum around rated-wind speed following similar trend as surge motion. Linear wave theory underestimates tension response when the waves become large. Moreover, mooring line tension tends to be quite non-Gaussian at large sea states while other response processes appear to be quite Gaussian. In extreme conditions, Gumbel fitting method and ACER method are used to predict the extreme value of some responses and both of them are able to give similar estimations. Linear wave generally underestimates wave elevation, floater surge motion and mooring line tension compared with fully nonlinear wave by 10%, 25% and 25% respectively.

The fatigue damage level at tower base is mainly wind dominating with outstanding result when tower natural mode is excited. Below rated wind speed, the fatigue level of mooring line is primarily governed by wind. When wind speed goes above rated wind speed where wave normally is large too, the contribution from wave becomes considerable and so is the wave nonlinearity effect.

In conclusion, nonlinear wave kinematics is important to consider in the design and analysis for floating wind turbine especially regarding predicting the fatigue damage at high sea states in operational condition and the extreme value of wave elevation, floater surge motion and mooring line tension in extreme condition.

Acknowledgement

References

[1] R. Gibson, C. Swan, The evolution of large ocean waves: the role of local and rapid spectral changes, Proc. R. Soc. A: Math. Phys. Eng. Sci. 463 (2006) 21–48.

[2] G.G. Stokes, On the Theory of Oscillatory Waves. Volume 1 of Cambridge Library Collection – Mathematics, Cambridge University Press, 2009, pp. 197–229.

[3] T. Camp, M. Morris, R. van Rooij, J. van der Tempel, M. Zaaijer, A. Henderson, K. Argyriadis, S. Schwartz, H. Just, W. Grainger, D. Peace, Design Methods for Offshore Wind Turbines at Exposed Sites, The European Commission, 2003 Technical Report.

[4] S. Schløer, H. Bredmose, H.B. Bingham, The influence of fully nonlinear wave forces on aero-hydro-elastic calculations of monopile wind turbines, Mar. Struct. 50 (2016) 162–188.

[5] H. Li, J. Du, S. Wang, M. Sun, A. Chang, Investigation on the probabilistic distribution of mooring line tension for fatigue damage assessment, Ocean Eng. 124 (2016) 204–214.

[6] L. Li, Z. Cheng, Z. Yuan, Y. Gao, Short-term extreme response and fatigue damage of an integrated offshore renewable energy system, Renew. Energy 126 (2018) 617–629.

[7] K. Xu, Y. Shao, Z. Gao, T. Moan, A study on fully nonlinear wave load effects on floating wind turbine, J. Fluids Struct. 88 (2019) 216–240.

[8] A. Robertson, J. Jonkman, M. Masciola, H. Song, A. Goupee, A. Coulling, C. Luan, Definition of the Semisubmersible Floating System for Phase II of OC4, National Renewable Energy Lab. (NREL), Golden, CO (United States), 2014 Technical Report.

[9] T.J. Larsen, A.M. Hansen, How 2 hawc2, The User's Manual, (2007).

[10] J. Mann, Wind field simulation, Probab. Eng. Mech. 13 (1998) 269–282.

[11] Y.L. Shao, O.M. Faltinsen, Towards efficient fully-nonlinear potential-flow solvers in marine hydrodynamics, ASME 2012 31st International Conference on Ocean, Offshore and Arctic Engineering, American Society of Mechanical Engineers, 2012, pp. 369–380.

[12] Y.L. Shao, O.M. Faltinsen, A harmonic polynomial cell (hpc) method for 3d laplace equation with application in marine hydrodynamics, J. Comput. Phys. 274 (2014) 312–332.

[13] H. Liang, O.M. Faltinsen, Y.L. Shao, Application of a 2d harmonic polynomial cell (hpc) method to singular flows and lifting problems, Appl. Ocean Res. 53 (2015) 75–90.

[14] Z. Gao, T. Moan, Frequency-domain fatigue analysis of wide-band stationary gaussian processes using a trimodal spectral formulation, Int. J. Fatigue 30 (2008) 1944–1955.

[15] M.I. Kvittem, T. Moan, Time domain analysis procedures for fatigue assessment of a semi-submersible wind turbine, Mar. Struct. 40 (2015) 38–59.

[16] API, 2sk, Recommended Practice for Design and Analysis of Stationkeeping Systems for Floating Structures, American Petroleum Institute, 1996.

[17] A. Næss, T. Moan, Stochastic Dynamics of Marine Structures, Cambridge University Press, 2013.

[18] P. Fu, B.J. Leira, D. Myrhaug, Reliability analysis of wake-induced collision of flexible risers, Appl. Ocean Res. 62 (2017) 49–56.

[19] A. Næss, O. Gaidai, Estimation of extreme values from sampled time series, Struct. Saf. 31 (2009) 325–334.

[20] Z. Cheng, H.A. Madsen, W. Chai, Z. Gao, T. Moan, A comparison of extreme structural responses and fatigue damage of semi-submersible type floating horizontal and vertical axis wind turbines, Renew. Energy 108 (2017) 207–219.

[21] P. Fu, B.J. Leira, D. Myrhaug, Assessment of methods for short-term extreme value analysis of riser collision, ASME 2018 37th International Conference on Ocean, Offshore and Arctic Engineering, American Society of Mechanical Engineers, 2018.

[22] K. Johannessen, T.S. Meling, S. Haver, et al., Joint distribution for wind and waves in the northern north sea, The Eleventh International Offshore and Polar Engineering Conference, International Society of Offshore and Polar Engineers, 2001.

[23] IEC, Iec 61400-3: Wind Turbines Part 3: Design Requirements for Offshore Wind Turbines, International Electrotechnical Commission, 2009.

[24] IEC, Iec 61400-1: Wind Turbines Part 1: Design Requirements, International Electrotechnical Commission, 2005.

[25] P.R. Thies, L. Johanning, V. Harnois, H.C. Smith, D.N. Parish, Mooring line fatigue damage evaluation for floating marine energy converters: field measurements and prediction, Renew. Energy 63 (2014) 133–144.